INTERNATIONAL JOURNAL FOR NUMERICAL METHODS IN FLUIDS
Int. J. Numer. Meth. Fluids 2007; **55**:965–983
Published online 11 April 2007 in Wiley InterScience (www.interscience.wiley.com). DOI: 10.1002/fld.1492

Numerical simulation of two-dimensional laminar slot-jet impingement flows confined by a parallel wall

A. Sivasamy[1,*,†,‡], V. Selladurai[2,§] and P. Rajesh Kanna[3,‡]

[1]*Department of Mechanical Engineering, Sri Krishna College of Engineering and Technology, Coimbatore, India*
[2]*Department of Mechanical Engineering, Coimbatore Institute of Technology, Coimbatore, India*
[3]*School of Building and Mechanical Sciences, Vellore Institute of Technology, Vellore, India*

SUMMARY

Two-dimensional laminar incompressible impinging slot-jet is simulated numerically to gain insight into flow characteristics. Computations are done for vertically downward-directed slot-jets impinging on a plate at the bottom and confined by a parallel surface on top. The behaviour of the jet with respect to aspect ratio (AR) and Reynolds number (Re) are described in detail. The computed flow patterns for various AR (2–5) and for a range of jet-exit Reynolds numbers (100–500) are analysed to understand the flow characteristics. The transient development of the flow is also simulated for AR $= 4$ and $Re = 300$. It is found that the reattachment length is dependent on both AR and Reynolds number for the range considered. The correlation for reattachment length is suggested. The maximum resultant velocity V_{rmax} and its trajectory is reported. A detailed study of horizontal velocity profile at different downstream locations is reported. It is found that the effect of Reynolds number and AR is significant to the bottom wall vorticity in the impingement and wall jet regions. Copyright © 2007 John Wiley & Sons, Ltd.

Received 13 September 2006; Revised 21 February 2007; Accepted 21 February 2007

KEY WORDS: slot-jet impingement; laminar flow; reattachment length

1. INTRODUCTION

Impinging jets are used in applications where high convective heat transfer rate is required. The local heat transfer coefficient is high in the impingement and adjoined wall jet region. Impinging jets are used to heat, cool, and dry the surfaces in number of industrial applications. They are employed in gas turbine cooling, tempering of glass, anti-icing of aircraft wings, drying of continuous sheets like papers, textiles, photographic films, and plywood, etc.

*Correspondence to: A. Sivasamy, Department of Mechanical Engineering, Sri Krishna College of Engineering and Technology, Coimbatore, India.
†E-mail: a_sivasamy@yahoo.com
‡Senior Lecturer.
§Professor.

Impinging jets are also used for cooling of microelectronic components where intense cooling is required over small areas. In microelectronic cooling, air velocities are small and, hence, the laminar regime is relevant for investigation [1]. The low Reynolds number jets are preferred in order to avoid high pressure in the impingement region. In recent years, many researches have carried out numerical and experimental investigations of impinging jet under various conditions. Single or multiple jets with cross-sections of round, annulus or slot-jets with or with out confinement surface are considered for investigations.

Sparrow and Wong [2] employed naphthalene sublimation technique to analyse mass transfer coefficients due to an impinging slot-jet in the laminar region. A mass-heat transfer analogy was used to convert mass transfer results into heat transfer results. Masliyah and Nguyen [3] studied the problem using holographic technique. Law and Masliyah [4] studied experimentally and theoretically the local mass transfer due to impingement of a confined laminar two-dimensional air jet on a flat surface for a Reynolds number up to 400 and for two jet-to-plate spacings. The experimental study was made *via* double exposure and real-time holography. Chen *et al*. [5] reported the experimental and numerical results for the high Schmidt number mass transfer to a line electrode in laminar impinging slot-jet flows. Slot-based Reynolds numbers from 220 to 690 were considered for the study.

Lin *et al*. [6] experimentally studied the heat transfer behaviours of a confined slot-jet impingement in laminar and transitional/turbulent regimes. The parametric effect of jet Reynolds number and jet separation distance on heat transfer characteristics of the heated target surface were studied. Al-Sanea [7] presented numerical results for laminar slot-jet impinging on an isothermal surface for three cases, namely, free-jet impingement, semi-confined jet impingement, and semi-confined jet impingement through a cross-flow. It was found that cross-flow degrades the nominal heat transfer rate.

San *et al*. [8] reported experimental results for a confined circular air jet impinging a surface with constant heat flux. The jet flow after impingement was constrained to exit in two opposite directions. Four diameter of impinging jet 3, 4, 6, and 9 mm and the jet Reynolds number range of 30 000–67 000 were considered. Baonga *et al*. [9] presented experimental results of the hydrodynamic and the thermal characteristics of free liquid jet impinged on a heated disk. Chou and Hung [10] reported numerical results of confined slot-jet impinging on isothermal surface. The effect of jet Reynolds number, ratio of separation distance to jet width, and jet velocity profile on stagnation and local heat transfer characteristics were explored. Nusselt number correlations were presented for predicting stagnation and local heat transfer characteristics. Rajesh Kanna and Das [11] numerically studied impingement region developed due to offset jet with respect to offset ratio and Reynolds number. Steady and unsteady analysis of impinging jet from rectangular slot in laminar flow has been presented by Chiriac and Ortega [1]. Chung and Luo [12] and Chung *et al*. [13] studied the unsteady impinging slot-jet using direct numerical simulation for low Reynolds number and presented the influence of primary vortex on flow field and stagnation Nusselt number.

Fitzgerald and Garimella [14] experimentally studied the flow field of an axisymmetric, confined, submerged, turbulent jet impinging normally on a flat plate. Reynolds number range of 8500–23 000 were considered. A recirculation zone was observed moving radially outwards from stagnation zone, with an increase in both Reynolds number and nozzle-to-plate spacing. Baydar [15] experimentally investigated the flow field between two horizontal surfaces arising from jet issuing from the lower surface and impinging normally on the upper surface. The effect of Reynolds number and nozzle-to-plate spacing on the flow structure were examined. It is reported that there exists a linkage between the subatmospheric region and peaks in heat transfer coefficients.

DOI: 10.1002/fld

A systematic comprehensive study for flow field of confined slot-jets for a wide range of low jet-exit Reynolds numbers and aspect ratios (AR) have not been done yet. In the present study, a time-marching incompressible flow solver has been applied for simulating the flow features of confined laminar impinging slot-jets for a range of AR and Reynolds number.

2. PROBLEM DESCRIPTION

An impinging slot-jet configuration sketch together with the definition of the relevant coordinates is shown in Figure 1. The jet comes from the top with uniform velocity and the impinging wall is located at $Y = 0$. A cartesian coordinate system centred at the stagnation point on impingement plate is used. X is the direction parallel to the impingement plate and Y is the negative jet direction. U and V are the corresponding horizontal and vertical velocity components. Only the right half of the domain is considered as the problem configuration is symmetrical with the axis of the rectangular slot.

The flow is assumed to be two dimensional, steady, isothermal, incompressible, and laminar in a cartesian reference frame. The fluid density and viscosity are assumed to be constant. Now the flow field can be described by a set of three partial differential equations, mass conservation, and

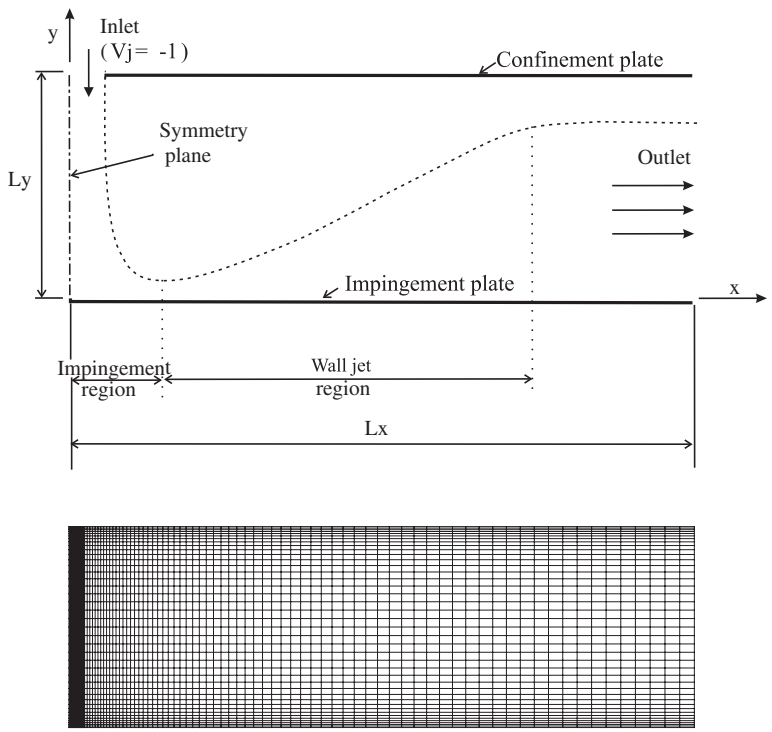

Figure 1. Schematic diagram of the problem configuration and representative grid.

DOI: 10.1002/fld

two momentum, given in non-dimensional form as

$$\frac{\partial U}{\partial X}+\frac{\partial V}{\partial Y}=0 \tag{1}$$

$$\frac{\partial U}{\partial t}+U\frac{\partial U}{\partial X}+V\frac{\partial U}{\partial Y}=-\frac{\partial P}{\partial X}+\frac{1}{Re}\left(\frac{\partial^2 U}{\partial X^2}+\frac{\partial^2 U}{\partial Y^2}\right) \tag{2}$$

$$\frac{\partial V}{\partial t}+U\frac{\partial V}{\partial X}+V\frac{\partial V}{\partial Y}=-\frac{\partial P}{\partial Y}+\frac{1}{Re}\left(\frac{\partial^2 V}{\partial X^2}+\frac{\partial^2 V}{\partial Y^2}\right) \tag{3}$$

where U and V are the velocity components in the X and Y directions, respectively, and P is the pressure. The scaling parameters are chosen as the uniform velocity at the jet exit, V_j, the hydraulic diameter of the jet, D_h, and ρV_j^2 as the characteristic pressure. The jet-exit Reynolds number, Re, is defined as $\rho V_j D_h/\mu$, ρ, and μ being the fluid density and viscosity, respectively. In arriving at Equations (1)–(3) from their dimensional form, the following non-dimensional variables are defined:

$$X=\frac{x}{D_h},\quad Y=\frac{y}{D_h},\quad U=\frac{u}{V_j},\quad V=\frac{v}{V_j},\quad t=\frac{t^* V_j}{D_h},\quad P=\frac{p}{\rho V_j^2}$$

where u and v are the dimensional velocity components in the x and y directions, respectively, and p is the dimensional local pressure.

The transient terms in Equations (2)–(3) are retained for marching the discretized equations to their asymptotic steady-state solutions from the given initial conditions.

A numerical model based on the vorticity-stream function formulation is developed. For this purpose, a non-dimensional vorticity ω is defined as

$$\omega=\frac{\partial V}{\partial X}-\frac{\partial U}{\partial Y} \tag{4}$$

and Equations (1)–(3) are reduced to a single vorticity-transport equation given by

$$\frac{\partial \omega}{\partial t}+U\frac{\partial \omega}{\partial X}+V\frac{\partial \omega}{\partial Y}=\frac{1}{Re}\left(\frac{\partial^2 \omega}{\partial X^2}+\frac{\partial^2 \omega}{\partial Y^2}\right) \tag{5}$$

A stream function ψ that satisfies the mass conservation equation, Equation (1), is defined such that

$$U=\frac{\partial \psi}{\partial Y},\quad V=-\frac{\partial \psi}{\partial X} \tag{6}$$

From Equations (4) and (6), the stream function equation is written as

$$\nabla^2 \psi=-\omega \tag{7}$$

Since vorticity is a scalar in a two-dimensional flow, the number of variables is now reduced to two, viz., the vorticity ω, and the stream function ψ. After solving the stream function, the

DOI: 10.1002/fld

velocity components U and V are calculated through Equation (6). The pressure field is not sought in this study.

The boundary conditions at the jet exit are specified as $U=0$ and $V=-1$. The no-slip boundary condition is followed in the top and bottom walls.

The computational domain length is extended long enough to attain a fully developed velocity profile at the exit. The following boundary conditions are used at the exit [16].

$$\frac{\partial^2\psi}{\partial X^2}=0, \quad \frac{\partial\omega}{\partial X}=0, \quad \frac{\partial U}{\partial X}=0, \quad \frac{\partial V}{\partial X}=0$$

3. NUMERICAL PROCEDURE

The convective terms in the vorticity-transport equation are discretized with upwind differencing. This is required for numerical stability. The diffusion terms are discretized with central difference scheme. The complete procedure can be found in [17] where convective terms are discretized using central difference scheme. The equation is solved by the alternating direction implicit (ADI) scheme. The stream function equation is solved by the successive over relaxation (SOR) method. Roache [18] gives a thorough discussion of the ADI and SOR schemes.

In the X direction upto jet width the grids are arranged uniform after being clustered. In the Y direction grids are clustered near the top and bottom walls. A systematic grid refinement study is conducted to obtained grid-independent solutions. The grid refinement study is presented in Table I. Computations are performed for the AR 5 at Re 100 and 500 for various grid refinement levels as shown in Table I. The convergence of the average skin friction coefficient at the bottom wall with grid refinement is shown in Figure 2. It is observed that grid refinement level 4 (231×121) produced almost grid-independent results and thus grid refinement level 4 is used for the entire computations.

Validation of the results against experiment could not be done because of the lack of suitable experimental data on this problem considered for the investigation. However the numerical results of the study by Sahoo and Sharif [19] and Park *et al.* [20], whose geometry and flow parameters are quite similar to the present study are reproduced using the present code. Sahoo and Sharif [19] used a different computational procedure (finite volume method with PISO algorithm). In Figure 3(a), the skin friction coefficient at the bottom wall predicted by the present computer code is compared with Sahoo and Sharif [19] for $Re=100$ and domain AR

Table I. Grid refinement scheme.

		X direction		Average C_f	
Grid refinement level	Y direction	$0 \leqslant X \leqslant 0.25$	$X > 0.25$	$Re=100$	$Re=500$
Grid 1	61	20	131	0.1981	0.0534
Grid 2	81	30	151	0.2007	0.0582
Grid 3	101	30	171	0.2043	0.0617
Grid 4	121	40	191	0.2067	0.0629
Grid 5	141	50	211	0.2081	0.0636

DOI: 10.1002/fld

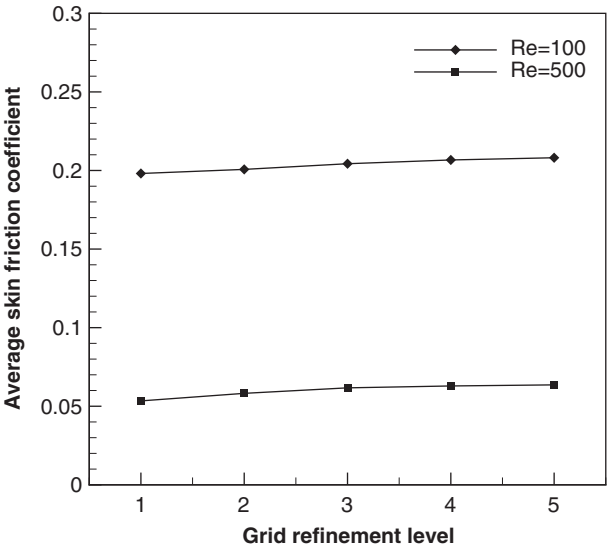

Figure 2. Convergence of average skin friction coefficient with grid refinement.

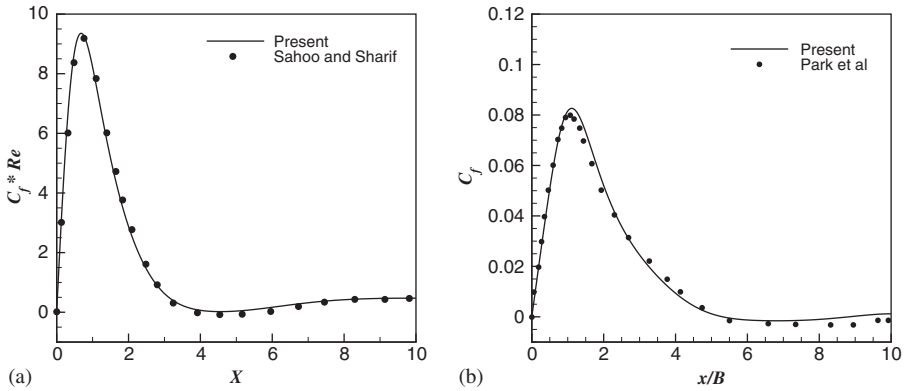

Figure 3. Comparison of the bottom wall skin friction coefficient C_f: (a) between the present study and those of Sahoo and Sharif [19] for $Re = 100$ and domain aspect ratio equals to 4 and (b) between the present study and those of Park *et al.* [20] for $Re = 220$ ($Re_{D_h} = 440$) and $H/B = 2$.

equals to 4. The agreement is found to be good. In Figure 3(b), the skin friction coefficient at the bottom wall predicted by the present computer code is compared with Park *et al.* [20]. (The solution obtained by QUICK scheme of FLUENT^{TM}) for $Re = 220$ ($Re_{D_h} = 440$) and $H/B = 2$. The agreement is found to be good in the impingement region and some discrepancy in skin friction coefficient is observed in the peak value and further downstream.

DOI: 10.1002/fld

4. RESULTS AND DISCUSSION

The jet width, W, is taken as 0.5 for the computations, so that the hydraulic diameter, D_h, becomes 1. The dimensionless domain length, L_x, is taken as 20 while the height, L_y, is varied. Four different values of L_y: 1, 1.5, 2, and 2.5 are considered which gives the AR, defined as L_y/W, of 2, 3, 4, and 5. The computations are done for five different jet-exit Reynolds numbers (100, 200, 300, 400, and 500), which is defined in terms of the hydraulic diameter and uniform exit velocity of the jet. The upper limit of 500 for Re is based on that suggested by Gauntner *et al*. [21] and Gardon and Akfirat [22] for laminar flow.

Chiriac and Ortega [1] reported that the flow is unsteady for $Re>650$ in the case of $H/W=5$. In the present study, the maximum Re is 500 and the maximum AR (L_y/W) is 5. Hence the steady flow and the symmetry boundary condition on the axis of the rectangular slot are assumed.

4.1. Primary and secondary vortex

Figure 4 depicts the location of primary and secondary vortexes. A counter-clockwise primary vortex is formed adjacent to the jet and below the confinement plate due to low-pressure formation near the mouth of the jet ejection. The flow is attached to confinement plate at the attachment point after impinging on the bottom plate. The reattachment length, X_1 (Figure 4) is the horizontal distance between the stagnation point and the attachment point.

The secondary vortex is formed when the momentum of the jet is unable to overcome the opposing frictional force of the impingement plate and retarding effects of the primary vortex. The distance between the stagnation point and the point at which the flow detaches from impingement plate is detachment length, X_2 (Figure 4).

4.2. Transient results

Figure 5 presents numerically simulated streamlines plot at various time levels for an AR of 4 and Re of 300. The time step 0.001 is used for the computation. The figure denotes that the initial action of the impinging jet that enters in the bulk fluid is similar to that of the free jet, entraining

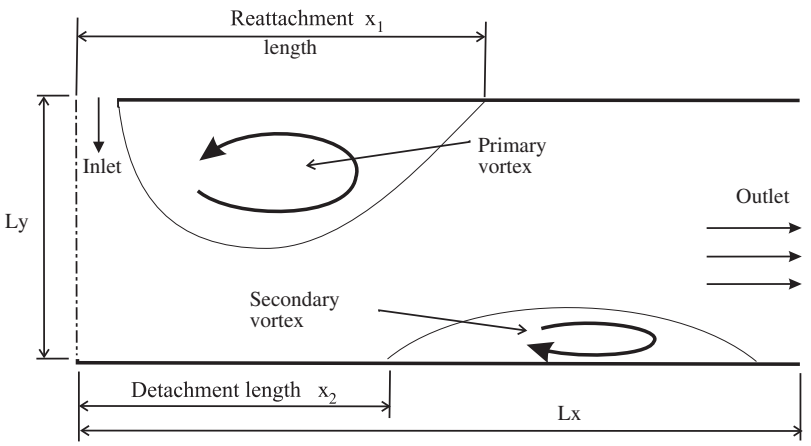

Figure 4. Definition of reattachment length and length of separation.

DOI: 10.1002/fld

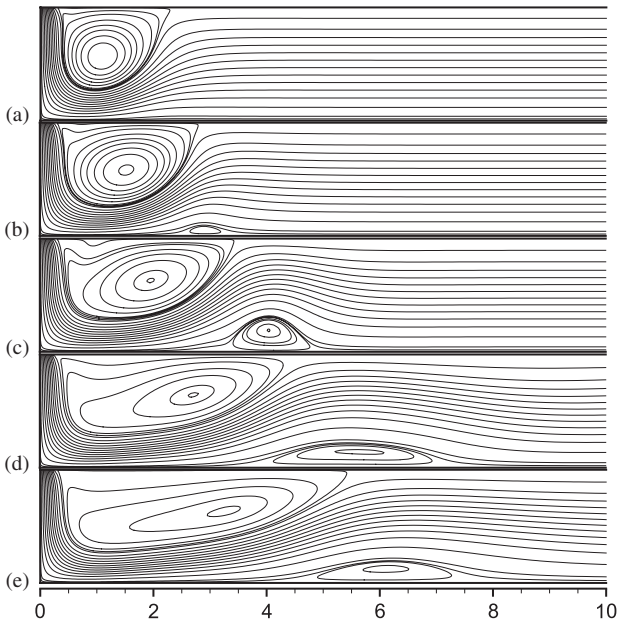

Figure 5. Transient results for $Re = 300$ and AR = 4. Streamlines plot: (a) $t = 10$; (b) $t = 15$; (c) $t = 25$; (d) $t = 60$; and (e) $t = 400$.

the bulk fluid and forming the primary vortex at $t = 10$ (Figure 5(a)). The formation of secondary vortex in the impinging plate is shown in Figure 5(b) at time $t = 15$. The primary and secondary vortex grow and move downstream as time increases (Figure 5(c)). The growth of secondary vortex in the Y direction is prevented as the length of primary vortex increases with increase in time (Figure 5(d)). The flow achieves its steady state at $t = 400$ (Figure 5(e)).

The location of maximum resultant velocity along the X direction called as V_{rmax} trajectory is shown in Figure 6(a) for different time levels. It is observed that the length of wall jet region increases as the time increases. Figure 6(b) shows the V_{rmax} along its trajectory. It is noticed that the decay rate of V_{rmax} in wall jet region decreases with increase in time. The horizontal velocity profile along the Y direction at $X = 2.0$ is shown in Figure 6(c). It is observed that the thickness of wall jet decreases as the flow reaches the steady state due to the growth of primary vortex that pushes the flow towards the impinging plate. It is also observed that the magnitude of negative velocity near confinement plate decreases with increase in time as primary vortex moves downstream. Figure 6(d) shows the horizontal velocity profile along the Y direction at exit. It is noticed that the behaviour of the flow at exit is, as expected, typical of channel flow.

4.3. Steady-state results

Figure 7 illustrates the streamline plots for various Reynolds numbers and AR = 5. It can be noted from Figure 7 that the stream lines are denser throughout the impingement region. However, the streamlines are less denser near confinement plate in the downstream in order to satisfy the no-slip conditions along the walls. The streamlines become parallel at exit and indicates the fully developed flow, which is similar to that obtained in case of channel flow.

DOI: 10.1002/fld

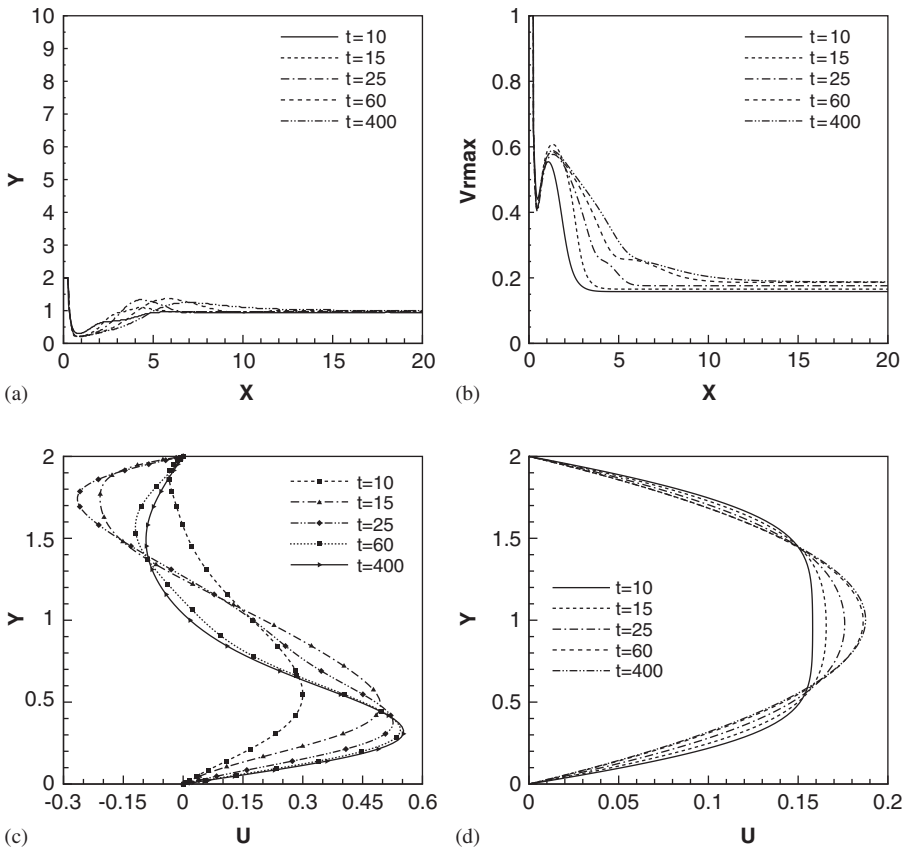

Figure 6. Transient results for $Re = 300$ and AR = 4: (a) V_{rmax} trajectory; (b) V_{rmax} along trajectory; (c) horizontal velocity profile at $X = 2.0$; and (d) horizontal velocity profile at exit.

It is observed that, there is a noticeable change in flow patterns due to change in location and size of vortexes as the Reynolds number changes for any particular AR. Figure 7 depicts that the size of the primary vortex increases while the Reynolds number is increased. It is also noticed that similar effect is obtained when AR is increased (Figure 8).

For larger Reynolds numbers and AR, flow separates from the impingement plate and forms a clockwise secondary vortex. It is weaker than primary vortex. The centre of secondary vortex moves downstream as Reynolds number increases (Figure 7(b–e)). It is noticed that similar effect is obtained when AR is increased (Figure 8(c,d)).

The location and the strength of the primary vortex are summarized in Table II for different Reynolds numbers and AR = 5. X_{pv} and Y_{pv} are the locations of the centre of primary vortex and ψ_{pv} is the stream function value at the centre of the primary vortex. The centre of primary vortex moves downstream while the Reynolds number is increased and there is a marginal upward movement in the Y direction. It is noticed that the strength of primary vortex decreases while Reynolds number is increased due to increase in size of the primary vortex.

DOI: 10.1002/fld

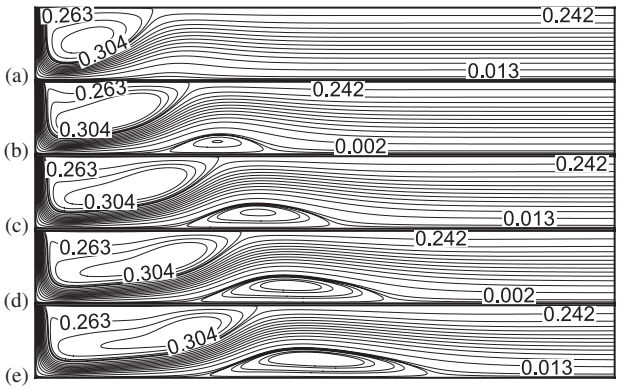

Figure 7. Streamlines plot of AR = 5 for various Reynolds numbers: (a) $Re = 100$; (b) $Re = 200$; (c) $Re = 300$; (d) $Re = 400$; and (e) $Re = 500$.

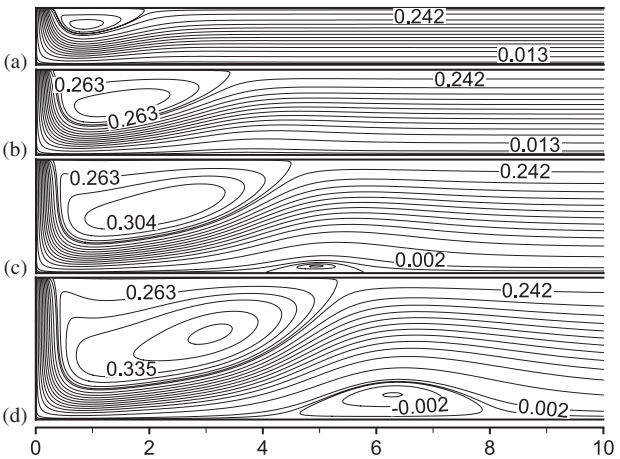

Figure 8. Streamlines plot of $Re = 200$ for various aspect ratios: (a) AR = 2; (b) AR = 3; (c) AR = 4; and (d) AR = 5.

The location and the strength of the primary vortex are summarized in Table III for different AR and $Re = 200$. The centre of primary vortex moves up and downstream as AR increases. It is interesting to note that the strength of primary vortex increases as AR increases.

The location and the strength of the secondary vortex are summarized in Table IV for different Reynolds numbers and AR = 5. X_{sv} and Y_{sv} are the locations of the centre of secondary vortex and ψ_{sv} is the stream function value at the centre of the secondary vortex. From Table IV, it is noticed that strength of secondary vortex increases while Reynolds number is increased. It is also observed that the centre of secondary vortex moves downstream while the Reynolds number is increased and there is a marginal upward movement in the Y direction.

DOI: 10.1002/fld

Table II. Centre of primary vortex: AR = 5.

Re	X_{pv}	Y_{pv}	ψ_{pv}
100	1.90	1.41	0.3735
200	3.07	1.49	0.3599
300	4.05	1.56	0.3468
400	4.84	1.63	0.3397
500	5.42	1.67	0.3356

Table III. Centre of primary vortex: $Re = 200$.

AR	X_{pv}	Y_{pv}	ψ_{pv}
2	0.87	0.70	0.2661
3	1.57	0.92	0.2983
4	2.44	1.22	0.3287
5	3.14	1.52	0.3600

Table IV. Centre of secondary vortex: AR = 5.

Re	X_{sv}	Y_{sv}	ψ_{sv}
100	—	—	—
200	6.26	0.44	−0.0030
300	7.66	0.55	−0.0064
400	8.83	0.62	−0.0088
500	9.65	0.69	−0.0106

4.4. Reattachment length

The dependency of the reattachment length with Reynolds number and AR is shown in Figure 9(a). The reattachment length has an increasing trend with Reynolds number with a falling rate of increase within the range of the considered Reynolds numbers. It is also noticed that similar effect is obtained for AR.

The following correlation is suggested to obtain the reattachment length for any given Reynolds number. The equation is fitted with the reattachment length using the nonlinear least-squares Marquardt–Levenberg algorithm

$$X_1 = C \times Re^m$$

The constants C and m in the equation are given in Table V for different AR. Comparison of reattachment length between numerical results and predictions with correlations are made and shown in Figure 9(b). Good agreements have been achieved between model and simulation.

The flow detaches from the impingement plate for larger AR at high Reynolds numbers. The detachment length of the secondary vortex is summarized in Table VI for different Reynolds

DOI: 10.1002/fld

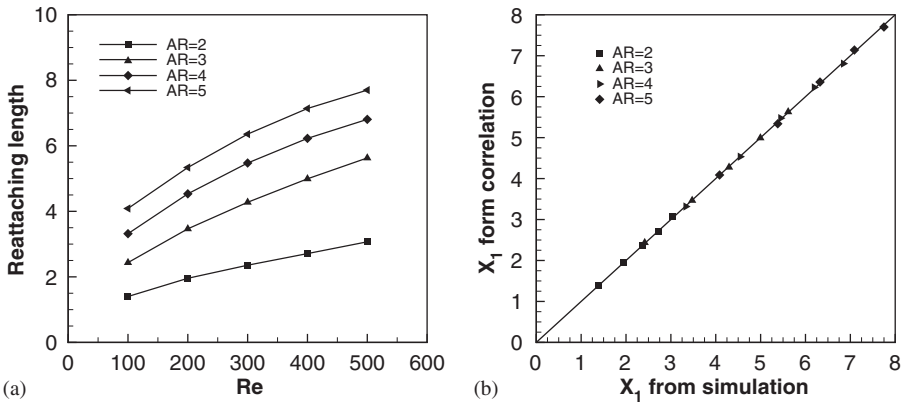

Figure 9. (a) Comparison of reattachment length with *Re* and AR. (b) Comparison of reattachment length between correlation and numerical results.

Table V. Constants for reattachment length equation.

AR	*C*	*m*
2	0.1476	0.4871
3	0.2167	0.5237
4	0.4255	0.4470
5	0.6544	0.3977

Table VI. Detachment length: AR = 5.

Re	X_2
100	—
200	4.3849
300	4.9098
400	5.3717
500	5.6843

numbers and AR = 5. It is noticed from Table VI that the detachment length increases when Reynolds number is increased.

4.5. Horizontal velocity contour

Entrainment occurs due to low pressure created near the mouth of the jet ejection when jet ejects into quiescent medium. The quiescent bulk fluid flows towards it and shear with main flow. The horizontal velocity contours are shown in Figure 10(a–e) for different Reynolds numbers and AR = 4. In the contours, the negative horizontal velocity near the jet ejection at inlet shows the bulk fluid flow towards low-pressure zone created by the ejection of the jet. In the contour

DOI: 10.1002/fld

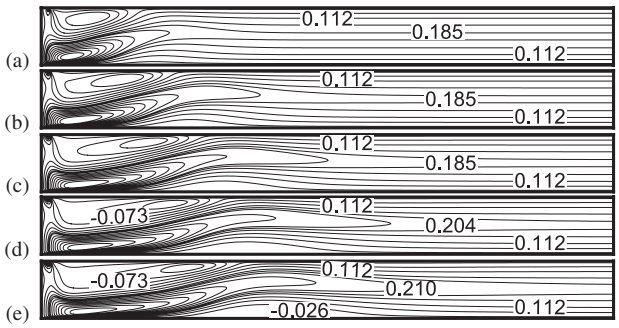

Figure 10. Horizontal velocity contour plot of AR = 4 for various Reynolds numbers: (a) $Re = 100$; (b) $Re = 200$; (c) $Re = 300$; (d) $Re = 400$; and (e) $Re = 500$.

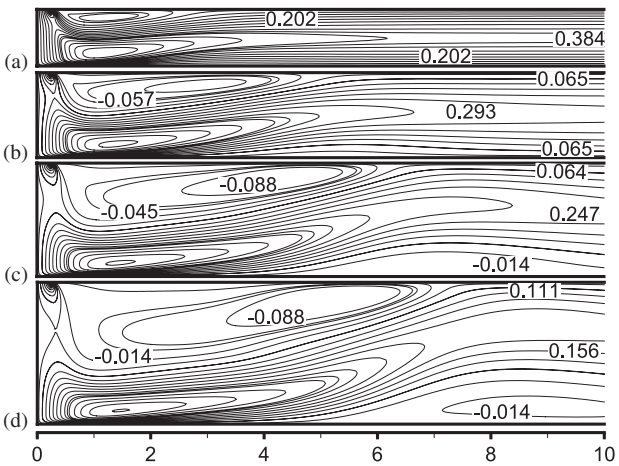

Figure 11. Horizontal velocity contour plot of $Re = 400$ for various aspect ratios: (a) AR = 2; (b) AR = 3; (c) AR = 4; and (d) AR = 5.

(Figure 10(e)), the negative horizontal velocity near the impingement plate shows the secondary vortex. Figure 11(a–d) shows the horizontal velocity contours for different AR and $Re = 400$.

4.6. Horizontal velocity profiles

Horizontal velocity profiles at different X for $Re = 100$ and AR = 5 are shown in Figure 12(a). The horizontal velocity profile makes a peak near impingement plate at location $X = 1.0$ which indicates the wall jet. The negative velocity profile near confinement plate indicates the formation of primary vortex. From the horizontal velocity profile at other downstream locations, it is seen that the wall jet expands in the Y direction and the magnitude of the velocity decreases as jet moves in streamwise direction. The parabolic horizontal velocity profile at exit indicates the fully developed flow condition.

DOI: 10.1002/fld

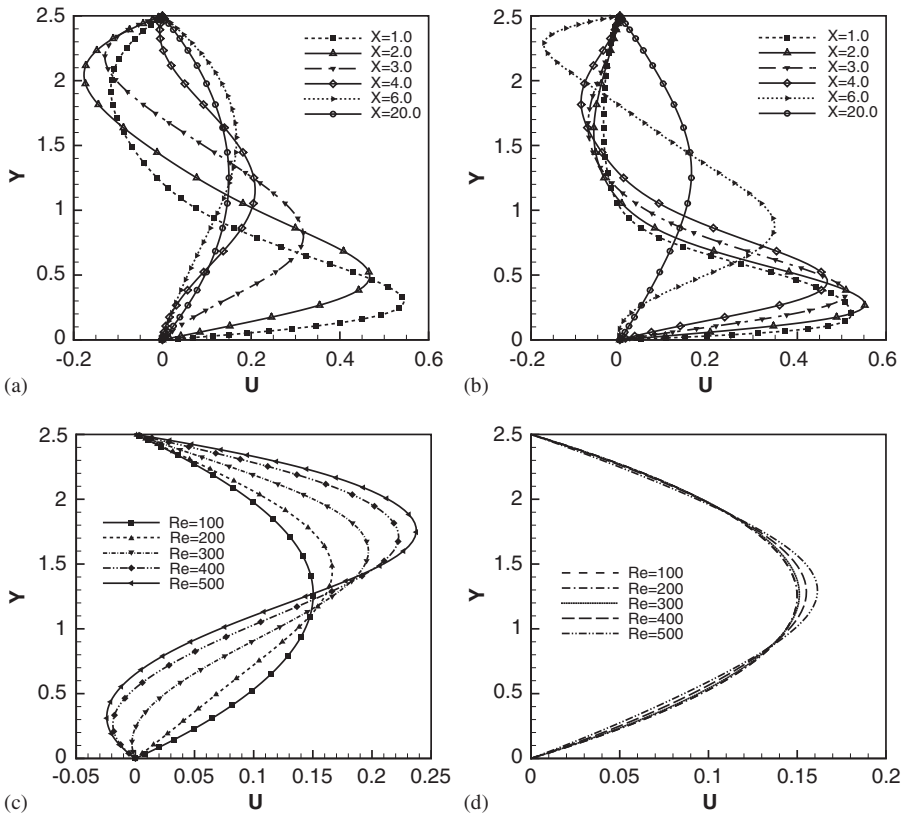

Figure 12. Horizontal velocity profiles for AR = 5: (a) at different X for $Re = 100$; (b) at different X for $Re = 500$; (c) at different Re for $X = 10$; and (d) at exit.

Horizontal velocity profiles at different X for $Re = 500$ and AR = 5 are shown in Figure 12(b). It is observed that the magnitude of horizontal velocity increases in the wall jet as Reynolds number increases. The negative horizontal velocity near impingement plate at $X = 6.00$ indicates the formation of secondary vortex. The wall jet at low Reynolds number spreads more in the Y direction at a particular location than that of a high Reynolds number (Figures 12(a) and (b)). It is due to the relatively less amount of momentum being carried by the fluid at lower Reynolds number.

Horizontal velocity profiles at $X = 10$ for different Reynolds number and AR = 5 are shown in Figure 12(c). It is noticed that the peak horizontal velocity increases and moves towards confinement plate as Reynolds number increases. The magnitude of negative horizontal velocity increases near impingement plate as Reynolds number increases. This indicates the increase in strength of secondary vortex.

Horizontal velocity profiles at exit for different Reynolds number and AR = 5 are shown in Figure 12(d). The parabolic horizontal velocity profile at exit indicates the fully developed flow condition. It is noticed that the peak horizontal velocity increases as Reynolds number increases.

DOI: 10.1002/fld

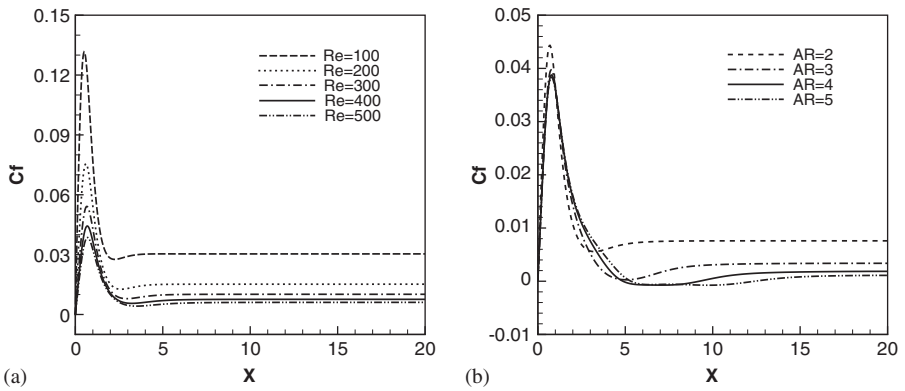

Figure 13. Comparison of skin friction coefficient: (a) AR = 2 and (b) $Re = 400$.

4.7. Skin friction coefficient

Figure 13(a) shows the variation of skin friction coefficient C_f, along the impingement plate for different Reynolds numbers and AR = 2. The local skin friction coefficient increases sharply from zero at the stagnation point to a maximum value in a short distance from stagnation point in the impingement region and then decreases in the streamwise direction. The skin friction coefficient is independent of X for any particular Reynolds number in further downstream. The skin friction coefficient decreases while Reynolds number is increased. In the impingement region, the horizontal velocity gradient in the Y direction increases with a falling rate of increase when Reynolds number increases. Hence, the skin friction coefficient decreases in this region when the Reynolds number increases.

Figure 13(b) shows the variation of skin friction coefficient C_f, along the impingement plate for different AR and $Re = 400$. For a given Reynolds number, the peak value of skin friction coefficient decreases with increase in AR. It is also observed that the effect of AR on skin friction coefficient decreases while AR increases.

4.8. Trajectory of maximum resultant velocity

The location of maximum resultant velocity, V_{rmax} ($V_r = \sqrt{u^2 + v^2}$) for the entire length of the domain known as V_{rmax} trajectory, is shown in Figure 14(a) for different Reynolds numbers and AR = 5. The location of V_{rmax} sharply falls down towards the impingement plate from the inlet of the jet in the impingement region. It gradually moves up in the wall jet region and reaches the peak near the confinement plate at the reattachment point and falls down gradually in further downstream. The location of V_{rmax} near the impingement plate moves close to it with a falling rate in the impingement region while the Reynolds number is increased. It is noticed that the length of wall jet region increases as Reynolds number increases due to increase in size of the primary vortex. The peak location of V_{rmax} near confinement plate increases as Reynolds number increases. The V_{rmax} trajectory becomes independent of Reynolds number near exit.

Figure 14(b) shows the comparison of trajectory of maximin resultant velocity for different AR and $Re = 500$. In the impingement region, the trajectory is not influenced by AR. The length of wall jet increases as AR increases for a particular Reynolds number due to increase in the size of

DOI: 10.1002/fld

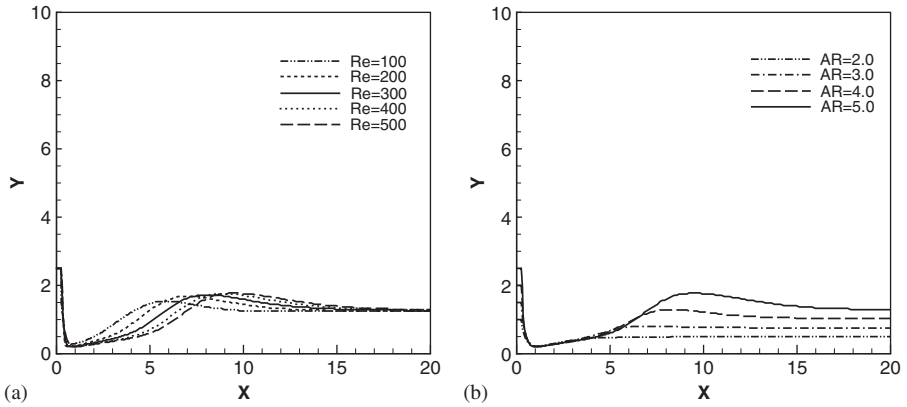

Figure 14. Comparison of V_{rmax} trajectory: (a) AR = 5 and (b) $Re = 500$.

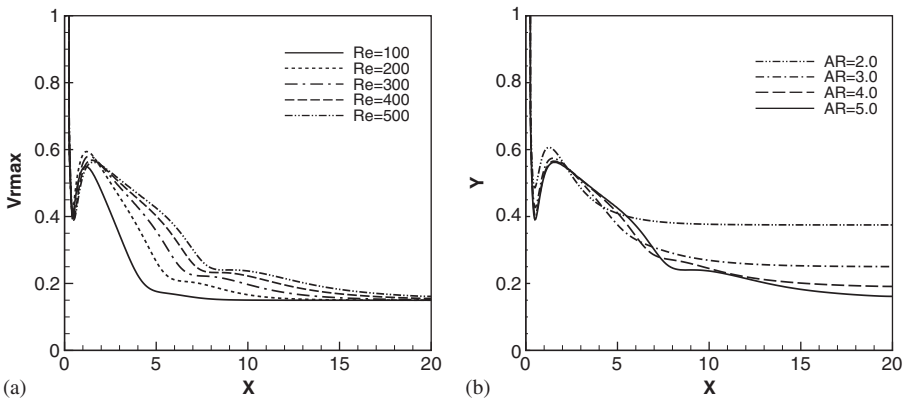

Figure 15. Comparison of V_{rmax} along trajectory: (a) AR = 5 and (b) $Re = 500$.

primary vortex. The peak location of V_{rmax} near confinement plate increases as AR increases. The trajectory is independent of X in further downstream.

4.9. Variation of maximum resultant velocity

Figure 15(a) shows the variation of maximum resultant velocity V_{rmax}, along its trajectory for different Reynolds numbers and AR = 5. The maximum resultant velocity sharply decreases from the jet inlet until the jet impinges the impingement plate. After impingement, resultant velocity increases sharply and reaches the peak value since the jet takes the turn and accelerates during impingement. From stagnation point to this peak point, the region is called as impingement region. Then, resultant velocity falls down gradually in the wall jet region as the main stream of flow expands in the Y direction. The main stream of flow hits the confinement plate and turns at the end of wall jet region. There is a small increase in resultant velocity due to turn and acceleration of fluid. The maximum resultant velocity gradually decreases in further downstream.

DOI: 10.1002/fld

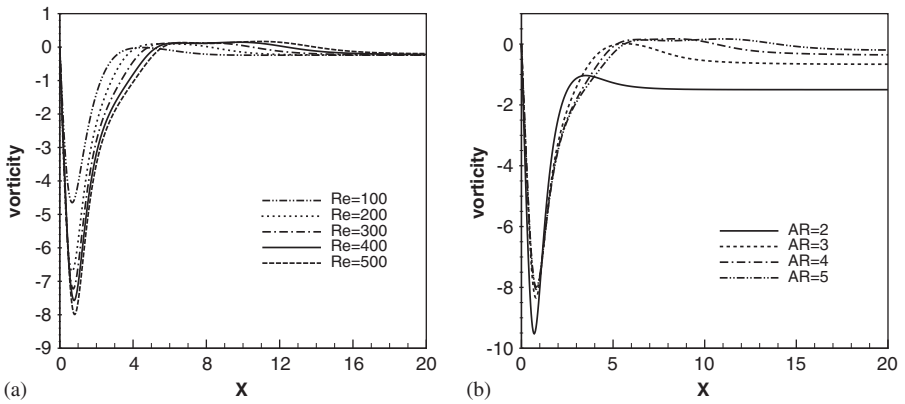

Figure 16. Vorticity distribution along the bottom wall: (a) AR = 5 and (b) $Re = 500$.

Figure 15(b) shows the variation of maximum resultant velocity V_{rmax}, along its trajectory for different AR and $Re = 500$. The drop in maximum resultant velocity, V_{rmax} increases with a falling rate as AR increases in the impingement region. The decay rate of V_{rmax} along its trajectory decreases as AR increases due to the increase in wall jet region. The drop in V_{rmax} in wall jet region increases with increase in AR due to the amount of momentum being carried by fluid decreases as the length of the wall jet increases.

4.10. Bottom wall vorticity

The bottom wall vorticity distribution for different Reynolds numbers and AR = 5 is shown in Figure 16(a). The vorticity variations are large in the impingement and wall jet regions and wall vorticity becomes independent of Reynolds number near exit. The magnitude of wall vorticity increases as Reynolds number increases in the impingement and wall jet regions and further downstream the wall vorticity is not much influenced by the increase in Reynolds number. The horizontal velocity gradient in the Y direction is increased in the impingement region while Reynolds number increases, which influences the vorticity in the negative direction.

Figure 16(b) shows the wall vorticity distribution for various AR and $Re = 500$. It is noticed that the effect of AR on wall vorticity decreases as AR increases. The magnitude of wall vorticity increases as AR decreases in the impingement region. The decay rate of wall vorticity decreases as AR increases in the wall jet region due to increase in the length of the wall jet region. The wall vorticity is independent of X for any particular AR in further downstream. It is also noticed that the wall vorticity vanishes at high AR (AR = 4 and 5) in the downstream.

5. CONCLUSION

Two-dimensional incompressible impinging slot-jet is solved by stream function and vorticity formulation considering the problem as asymptotic solution to the transient equation. The flow characteristics like reattachment length, strength of primary vortex, velocity profiles, impingement region, and wall jet region are studied in detail by varying Reynolds number and AR. The transient

DOI: 10.1002/fld

results show the nature of vortex generation, its movement with respect to time and attainment of the final steady-state solution. The primary vortex and secondary vortex grow as time increases and their centres move downstream and reaches a particular location. The size of the primary vortex formed due to entrainment increases with increase in Reynolds number and AR. The reattachment length has an increasing trend with a falling rate of increase within the range of considered Reynolds numbers and AR. The centre of primary vortex is significantly influenced by both the Reynolds number and AR. The strength of primary vortex decreases with an increase in Reynolds number and increases with increase in AR. The correlations for reattachment length is proposed for the range of Reynolds number (100–500) considered. The skin friction coefficient decreases with an increase in Reynolds number for any particular AR. The length of wall jet region increases with increase in Reynolds number and AR. The wall jet spreads more in the Y direction at low Reynolds number. The bottom wall vorticity is considerably affected in the impingement region and wall jet region for the change in Reynolds number and AR.

NOMENCLATURE

C_f	skin friction coefficient
D_h	hydraulic diameter of the jet (m)
L_x	dimensionless domain length
L_y	dimensionless domain height
p	pressure (N/m^2)
P	dimensionless pressure
Re	Reynolds number
t	dimensionless time
t^*	time (s)
u, v	velocity components (m/s)
U, V	dimensionless velocity components
V_j	jet exit velocity (m/s)
V_r	dimensionless resultant velocity
W	jet width (m)
x, y	space coordinates (m)
X, Y	dimensionless space coordinates

Greek symbols

μ	viscosity (kg/m s)
ρ	density (kg/m^3)
ψ	dimensionless stream function
ω	dimensionless vorticity

Subscript

max	maximum

ACKNOWLEDGEMENTS

The constructive comments and suggestions of the reviewers are sincerely acknowledged by the authors.

DOI: 10.1002/fld

REFERENCES

1. Chiriac VA, Ortega A. A numerical study of the unsteady flow and heat transfer in a transitional confined slot jet impinging on an isothermal surface. *International Journal of Heat and Mass Transfer* 2002; **45**:1237–1248.
2. Sparrow EM, Wong TC. Impingement transfer coefficients due to initially laminar slot jets. *International Journal of Heat and Mass Transfer* 1975; **18**:597–605.
3. Masliyah JH, Nguyen TT. Mass transfer due to an impinging slot jets. *International Journal of Heat and Mass Transfer* 1979; **22**:237–244.
4. Law H-S, Masliyah JH. Mass transfer due to a confined laminar impinging two-dimensional jet. *International Journal of Heat and Mass Transfer* 1984; **27**:529–539.
5. Chen M, Chalupa R, West AC, Modi V. High Schmidt mass transfer in a laminar impinging slot jet flow. *International Journal of Heat and Mass Transfer* 2000; **43**:3907–3915.
6. Lin ZH, Chou YJ, Hung YH. Heat transfer behavior of a confined slot jet impingement. *International Journal of Heat and Mass Transfer* 1997; **40**:1095–1107.
7. Al-Sanea S. A numerical study of the flow and heat transfer characteristics of an impinging laminar slot-jet including crossflow effects. *International Journal of Heat and Mass Transfer* 1992; **35**:2501–2513.
8. San J-Y, Huang C-H, Shu M-H. Impingement cooling of a confined circular air jet. *International Journal of Heat and Mass Transfer* 1997; **40**:1355–1364.
9. Baonga JB, Louahlia-Gualous H, Imbert M. Experimental study of the hydrodynamic and heat transfer of free liquid jet impinging a flat circular heated disk. *Applied Thermal Engineering* 2006; **26**:1125–1138.
10. Chou YJ, Hung YH. Impingement cooling of an isothermally heated surface with a confined slot jet. *Journal of Heat Transfer* 1994; **116**:2137–2145.
11. Rajesh Kanna P, Das MK. Numerical simulation of two-dimensional laminar incompressible offset jet flows. *International Journal for Numerical Methods in Fluids* 2005; **49**:439–464.
12. Chung YM, Luo KH. Unsteady heat transfer analysis of an impinging jet. *Journal of Heat Transfer* 2002; **124**:1039–1048.
13. Chung YM, Luo KH, Sandham ND. Numerical study of momentum and heat transfer in unsteady impinging jets. *International Journal of Heat and Fluid Flow* 2002; **23**:592–600.
14. Fitzgerald JA, Garimella SV. Flow field effect on heat transfer in confined jet impingement. *Journal of Heat Transfer* 1997; **119**:630–635.
15. Baydar E. Confined impinging air jet at low Reynolds numbers. *Experimental Thermal and Fluid Science* 1999; **19**:27–33.
16. Rajesh Kanna P, Das MK. A short note on the entrainment and exit boundary conditions. *International Journal for Numerical Methods in Fluids* 2006; **50**:973–985.
17. Rajesh Kanna P. Flow and conjugate heat transfer study of wall bounded laminar plane jet flows. *Ph.D. Thesis*, Indian Institute of Technology, Guwahati, 2005.
18. Roache PJ. *Computational Fluid Dynamics* (revised edn). Hermosa: Albuquerque, NM, 1982.
19. Sahoo D, Sharif M. Numerical modeling of slot-jet impingement cooling of a constant heat flux surface confined by a parallel wall. *International Journal of Thermal Sciences* 2004; **43**:877–887.
20. Park TH, Choi HG, Yoo JY, Kim SJ. Streamline upwind numerical simulation of two-dimensional confined impinging slot jets. *International Journal of Heat and Mass Transfer* 2003; **46**:251–262.
21. Gauntner J, Livingwood J, Hrycak P. Survey of literature on flow characteristics of a single turbulent jet impinging on a flat plate. *NASA TN D-5652*.
22. Gardon R, Akfirat J. Heat transfer characteristics of impinging two-dimensional air jets. *Journal of Heat Transfer* 1966; **88**:101–108.

DOI: 10.1002/fld